

# Experimental-Numerical Analysis of Thin-Walled Box Structures Stiffened with Corrugated Ribs, Subjected to Torsion

Tomasz Kopeccki<sup>1</sup>, Przemysław Mazurek<sup>1</sup>

<sup>1</sup> Department of Mechanical Engineering and Aviation, Rzeszów University of Technology, Al. Powstańców Warszawy 8, Rzeszów, Poland

\* Corresponding author's e-mail: [tkopeccki@prz.edu.pl](mailto:tkopeccki@prz.edu.pl)

## ABSTRACT

The study presented the results of model experimental investigations on box structures made using additive manufacturing. The examined models had walls with reinforcements in the form of corrugations. An experiment was also conducted using a reference model without stiffeners. The aim of the study was to determine the influence of corrugation geometry on the shape and magnitude of structure deformations, as well as on the level of critical loads. The experiments were conducted using a dedicated research stand. Nonlinear numerical analyses of selected structure variations were also carried out using finite element method-based software. A comparison of the maximum displacement values obtained by experimental and numerical methods was made.

**Keywords:** thin-walled structures, 3D printing, torsion, experiment, finite elements method, stiffeners.

## INTRODUCTION

Thin-walled load-bearing structures reinforced with corrugations have been a structural solution long used in aerospace engineering. During the late pioneering era, when designers lacked sufficient knowledge about the influence of stability loss on the material state of the shell, efforts were made to prevent this effect by using corrugated sheet covers. Examples of this approach can be found in the designs of Junkers or Stout.

In a later period, as research in aeronautical engineering reached a more advanced stage, smooth coverings began to be used, allowing for the occurrence of local and elastic buckling in operational conditions in some cases. However, in zones of the airframe serving key strength or aerodynamic functions, stability loss phenomena needed to be eliminated. Therefore, there was a drive to create an effective structural solution that would significantly increase levels of critical loads while maintaining mass limitations [1–3]. During the time when most aircraft constructions were metal-based, corrugations in the form of

ribs, implemented through plastic deformation, proved to be such a solution (Fig. 1). Currently, advancements in materials engineering allow for significant diversification in the technologies used to produce aerospace structural components [4]. In addition to the increasingly popular use of fiber composites, 3D printing technology [5] is also gaining interest among designers. Due to the nature of the manufacturing process, which is much easier compared to forming carbon-epoxy composites, it can be expected that in the relatively near future, additive manufacturing will become one of the most common methods for producing aerospace structures [6].

Regardless of the manufacturing technology, there will still be a need to ensure that structural components possess appropriate properties concerning critical load values [7]. Therefore, it can be assumed that solutions used for metallic structures could also be applicable to additive manufacturing. Corrugated reinforcements, as one such proven solution, deserve attention both in terms of manufacturing issues and mechanical properties.



**Figure 1.** An example of the application of embossing in the aircraft tail covering

Additive manufacturing offers significantly greater freedom in shaping reinforcements than is possible with plastic stamping. Therefore, it seems prudent to conduct research to determine the impact of reinforcement geometry details on the mechanical properties of the structure equipped with them. This paper presents the results of experiments conducted using a range of models with varied rib geometries, as well as a reference version with smooth walls. One of the models, produced using additive manufacturing, featured ribs with closed perimeters, equipped with additional enclosing walls. Numerical calculations were also performed to determine the distribution of critical zones in selected versions of the tested shells.

**PURPOSE AND SCOPE OF THE STUDY**

The subject of the research involved the walls of box structures with various geometric

configurations (Fig. 2). Experiments were conducted on a reference structure devoid of ribs and four types of structures featuring walls with rows of ribs. The top and bottom walls had a thickness of 6 mm and were equipped with reinforcements to facilitate attachment to the test rig. The front and rear walls, which were the focus of the research and analysis, had a thickness of 0.6 mm in all variants. Five structural variants were tested. Variant 1 corresponded to walls without ribs. The remaining variants differed in the shape of their cross-section (Fig. 3). In the last variant, ribs with closed perimeters were used.

The models for experimental studies were produced using additive manufacturing (Fig. 4). Polylactic acid filament (PLA) was used as the modeling material, as it offers a relatively broad range of elastic properties [8]. The components of the models, i.e., the top, bottom, side, and closing walls, were printed separately and then joined using adhesive connections. For Variant 5, it was

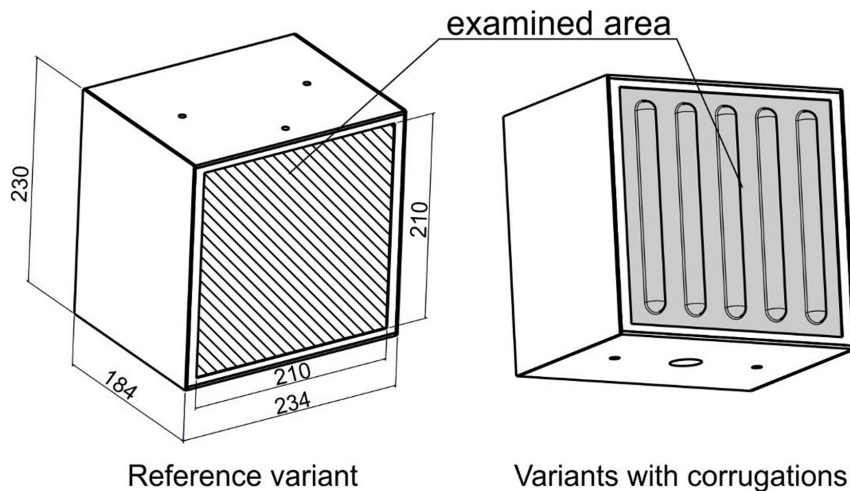


**Figure 2.** Geometric variants of the studied structure

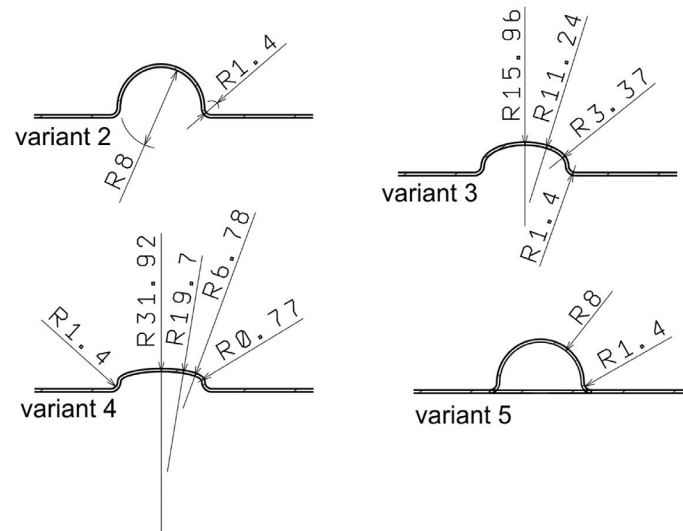


Figure 3. Variants of rib shapes

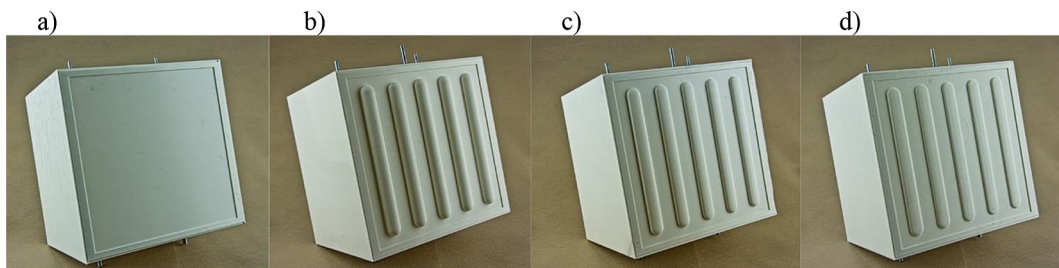


Figure 4. Experimental study models: (a) variant 1, (b) variant 2, (c) variant 3, (d) variant 4

necessary to create a series of ribs with closed perimeters that lacked infill. Due to the need for supports, polyvinyl alcohol filament (PVA), a water-soluble material, was used for their printing.

Each of the ribs had two small holes at the base to allow for the flushing out of the support structures that supported the main shell (Fig. 5). During the experiment, the top walls of the models were attached to a fixed plate on the test rig, while the

bottom walls were attached to a movable beam equipped with a bearing, which defined the torsion axis (Fig. 6). The load was applied gravitationally using a dedicated kinematic system.

Displacement measurements of the loading beam were conducted using a micrometer sensor. This allowed for determining the total torsion angle of the tested structure. Furthermore, an optical scanner ATOS, based on the structured light

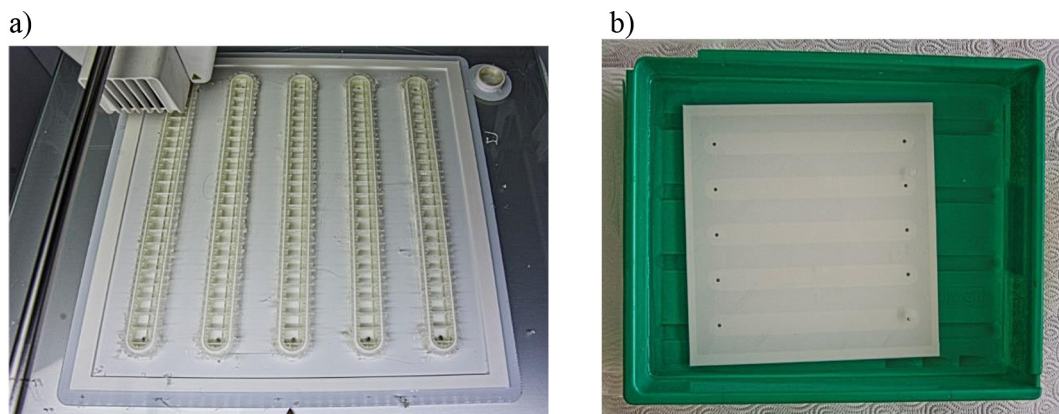


Figure 5. Model preparation process: (a) printed wall with closed ribs, (b) wall in the process of flushing out PVA

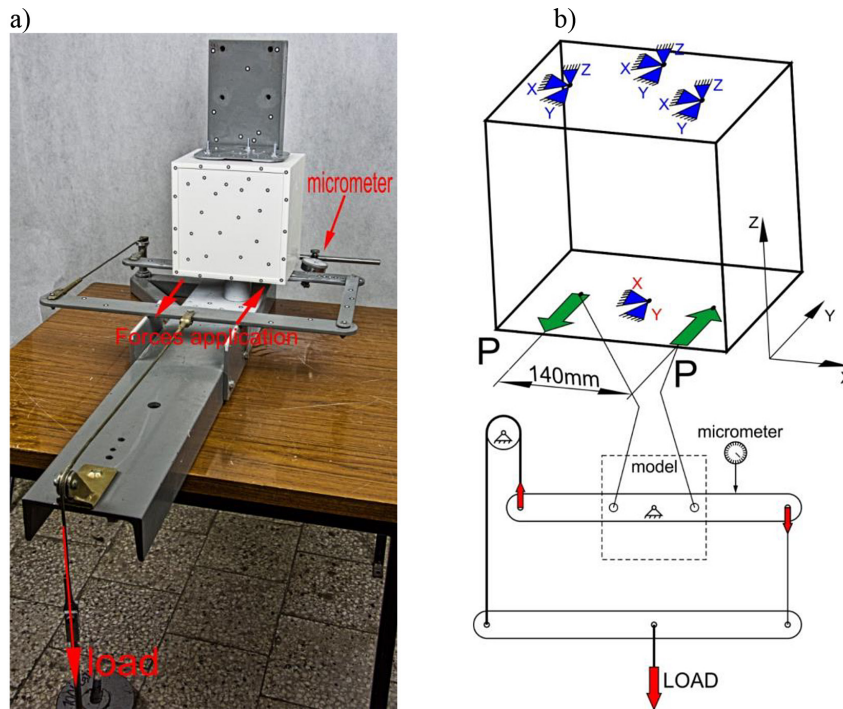


Figure 6. Experimental stand: (a) model on the test rig, (b) diagram of the loading-measuring system

method, was used for measuring the deformations of the structure walls (Fig. 7).

Next, numerical models of variants 1, 2, and 5 were created. Nonlinear numerical analyses were conducted using the MSC PATRAN/MARC software, which utilized the finite element method. The numerical calculations aimed to reveal the complex nature of stress distribution in the walls of the tested structures, as well as any potential undesired stress concentration zones.

## EXPERIMENTAL RESEARCH

The comparative analysis of the mechanical properties of the tested models required

establishing the relationship between the load on the structures and the corresponding quantity describing their current state. In general, such relationships, referred to as equilibrium paths, due to the multitude of degrees of freedom of real systems, would need to be hyper surfaces in a multi-dimensional state space, where the number of dimensions corresponds to the number of degrees of freedom of the structure. In practice, comparison of representative equilibrium paths is used, reducing the description of the structure's state to a single selected parameter. In the discussed case, the representative equilibrium paths were the relationships between the total torsion angle of the structure and the torsional moment (Fig. 8). For all tested models, the same range

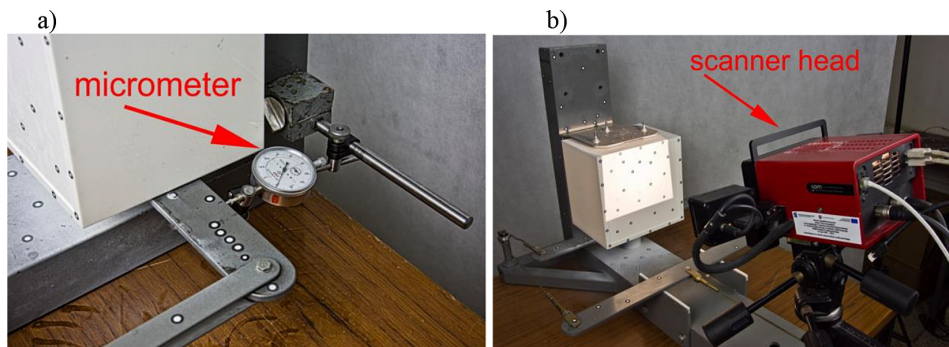


Figure 7. Details of the experiment: (a) measurement of torsion angle, (b) displacement measurement using an optical scanner

of loads was applied. The maximum force on the scale was 26.5 kN, equivalent to a torsional moment of 38.93 Nm. Subsequent displacement measurements were taken after each 1 kg increment in the scale’s mass, corresponding to an increase in the torsional moment on the structure by 1.45 Nm. Displacement distributions normal to the wall plane were determined for all model variants using the optical scanner (Fig. 9–13). For comparative purposes, scanning was performed for all cases when the scale mass reached 20 kg, corresponding to a torsional moment of 28.8 Nm.

In the case of the reference variant, instability within the studied area occurred early in the loading phase. Due to the presence of tension forces, the buckling had a stable nature, and the nonlinearity of the curve corresponded to the deepening of folds. At around 35 Nm of loading, in a highly

advanced deformation phase, an increase in the model’s stiffness was observed, resulting from the changing nature of the tension field and the predominant work of fibers being stretched in the diagonal area of the wall.

The use of ribs prevented the buckling effect of the shell. The largest displacements normal to the wall plane were observed in areas adjacent to the outer parts of the rib bases. However, as observed during the experiment, these displacements were not critical but resulted from the complex deformation of the entire wall. Deformation patterns determined through scanning indicated the torsion occurring in each of the ribs. Simultaneously, due to stretching and compression in the wall plane, the walls were deformed, resulting in a reduction in the overall torsional stiffness of the models compared to the reference variant.

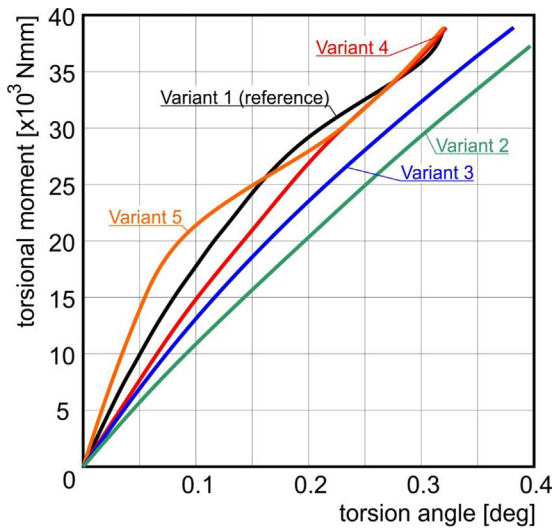


Figure 8. Representative equilibrium paths

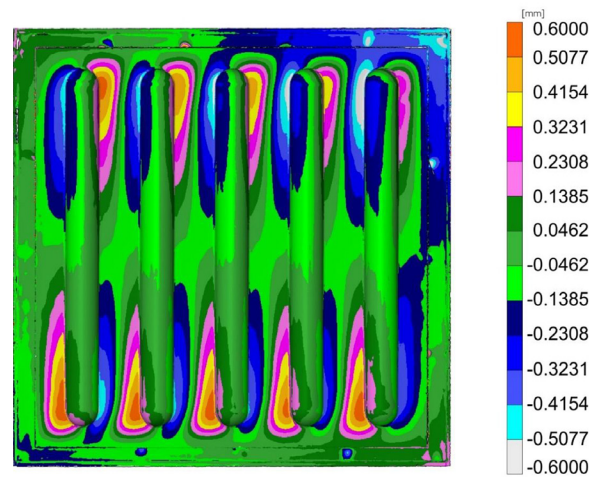


Figure 10. Displacement distribution normal to the wall plane [mm] – variant 2

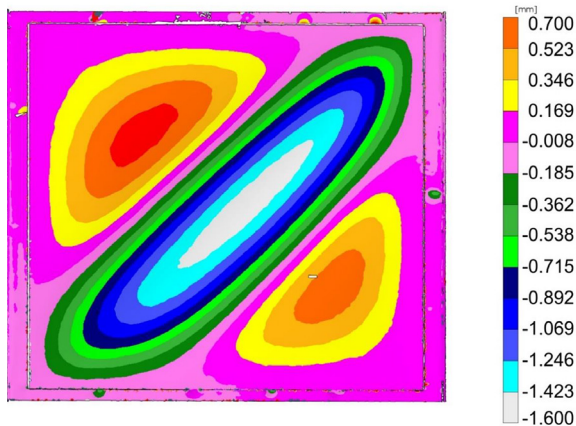


Figure 9. Displacement distribution normal to the wall plane [mm] – variant 1 (reference)

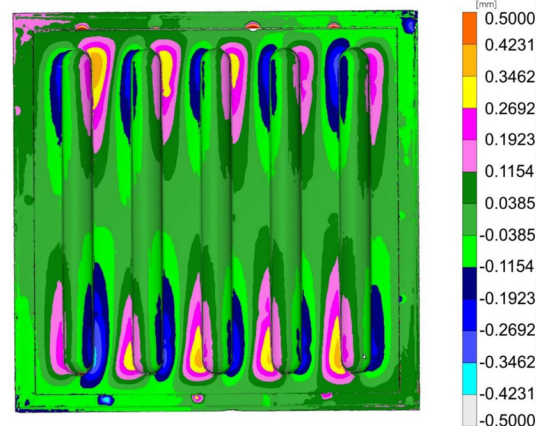
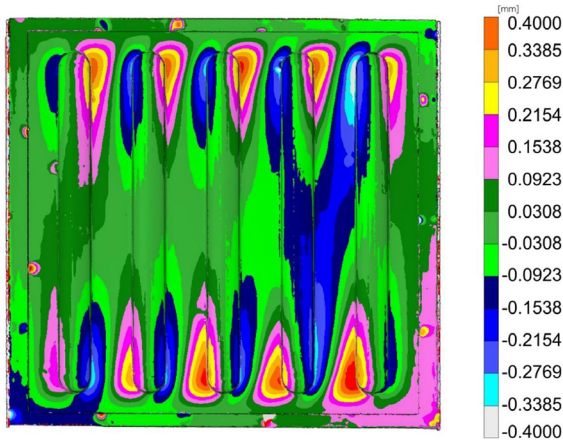
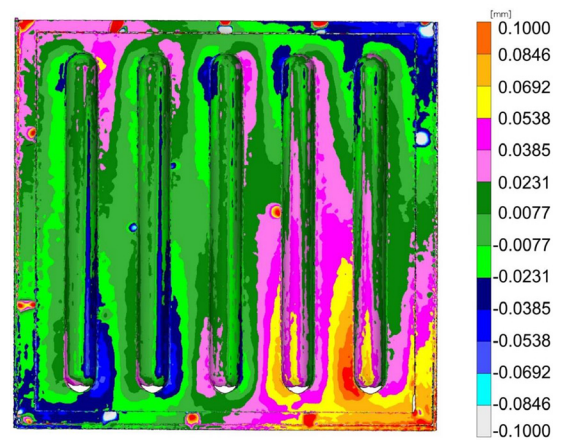


Figure 11. Displacement distribution normal to the wall plane [mm] – variant 3



**Figure 12.** Displacement distribution normal to the wall plane [mm] – variant 4



**Figure 13.** Displacement distribution normal to the wall plane [mm] – variant 5

As indicated by the course of the representative equilibrium paths, the decrease in overall torsional stiffness was greater the closer the shape of the rib cross-section resembled a semicircle. This corresponded to the increased ability for diagonal elongation of the wall during stretching. As the ribs flattened, there was an increase in the overall torsional stiffness. Simultaneously, the displacements normal to the wall plane decreased. The qualitative distribution of displacements in variants corresponding to open ribs (Variants 2, 3, 4) was very similar. However, quantitative results suggest that there is a geometric form of the rib cross-section, corresponding to an appropriate selection of its curvature, that could significantly increase the level of critical loads for the tested system while minimally reducing its overall torsional stiffness compared to the reference case. This could be a subject for further research within the discussed issues.

The use of ribs with closed cross-sections had a significant impact on both the displacement distribution pattern and the increase in the torsional stiffness of the structure. A comparison of the scan images revealed that the maximum displacements normal to the wall plane in Variant 5 were four times smaller than in Variant 4. This is due to the fact that a significant portion of the loads is transferred by the closing walls of the rib sections. The ribs themselves act as spacers in this case, preventing the instability of the wall. At the same time, they are thin-walled closed-profile sections with significant torsional stiffness. As a result, in the initial deformation phase, there was an approximately fifty percent increase in the torsional stiffness of the structure compared to the

reference case. It is important to note the clear deviation in the equilibrium path of Variant 5 at a load of approximately 20 Nm (Fig. 8). The most likely cause of this effect is the instability of the closing walls of the ribs. Although this is a local phenomenon, it has a significant impact on the torsional stiffness of the structure. Unfortunately, observing this during the experiment was not possible due to the model's construction. In similar cases, it seems advisable to conduct numerical analyses based on nonlinear procedures.

It should be emphasized that, as mentioned earlier, scanning in all cases was conducted with a torsional moment load of 28.8 Nm. In the case of Variant 5, this corresponded to a deformation phase where there was a decrease in the torsional stiffness of the structure, indicating an advanced buckling deformation of the closing rib walls. The research results lean towards considering further solutions regarding the use of corrugated ribs. The least sophisticated way to prevent the buckling of the closing walls would be to increase their thickness, which, in the case of the discussed structure, would not lead to a significant increase in its mass. However, it should be noted that in real aerospace constructions, with a large number of ribs, this increase could reach an undesirable level. An alternative solution is to use ribs with closed cross-sections but without flat walls (Fig. 14). In such a case, another series of experiments would be necessary to determine the influence of the geometry of the cross-section of the ribs on the displacement distribution within the walls and the overall torsional stiffness of the structure.

When discussing the advantages and disadvantages of the considered solutions, it is

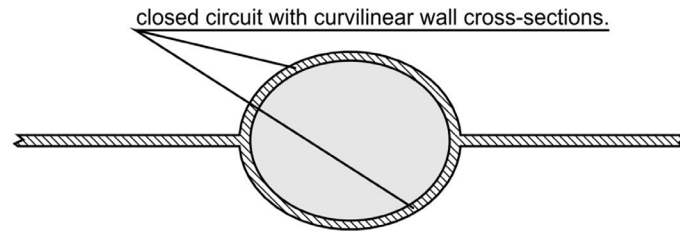


**Figure 14.** An example of a rib geometry with a closed cross-section, devoid of flat walls

important to take into account their mass. In the case of metal structures, ribs are formed as a result of plastic processing, and their presence does not affect the structure’s mass, unlike those shaped through additive manufacturing. Below is a comparison of the masses of the different wall variants (Table 1).

### NUMERICAL ANALYSES

To compare stress distributions, identify critical zones, and confirm the occurrence of buckling deformations in the closing rib walls, nonlinear numerical analyses of variants 1, 2, and 5 were conducted. The calculations were performed using MSC PATRAN/MARC software based on the finite element method.

The material constants of PLA were determined in separately conducted experiments [9]. Although the structure of the print is not entirely uniform, considering the relatively small differences between the mechanical properties in different directions of the printed layer, the assumption of linearly elastic, isotropic material properties was adopted to simplify calculations. The constants were respectively:  $E = 3300 \text{ MPa}$ ,  $\nu = 0.34$ .

The essence of nonlinear analysis is to determine the course of the equilibrium path of the system, which constitutes a hyper surface in a hyper state space [10–11] with a number of dimensions equal to the number of degrees of freedom

**Table 1.** Comparison of the masses of individual wall variants

| Variant | Mass [g] |
|---------|----------|
| 1       | 53       |
| 2       | 81       |
| 3       | 73       |
| 4       | 66       |
| 5       | 92       |

of the system. The analysis is conducted by performing a series of successive incremental steps associated with increased loading. In each step, the discrete system satisfies the residual force equation [12–14]:

$$r(u, \lambda) = 0 \tag{1}$$

In this equation,  $u$  represents the state vector, with components corresponding to the displacements of the structure’s nodes in its current geometric configuration.  $\lambda$  is the control parameter proportional to the load, and  $r$  is the residual vector containing the unbalanced force components corresponding to the current deformation state.

In the incremental phase, which involves transitioning from state  $n$  to state  $n + 1$ , the increments are not determined:

$$\Delta u_n = u_{n+1} - u_n, \Delta \lambda_n = \lambda_{n+1} - \lambda_n \tag{2}$$

In incremental-corrective procedures, there is also a corrective phase that allows for determining the above-mentioned quantities. This is an iterative procedure aimed at satisfying the system’s incremental control equation, also known as the constraint equation [15–17]:

$$c(\Delta u_n, \Delta \lambda_n) = 0 \tag{3}$$

which results from the corrective strategy adopted by the user.

For the discussed models, the predictive Newton-Raphson method was utilized, with a load correction phase. The numerical models were based on bilinear, four-node shell elements (Fig. 15–16). In the case of variant 2, the finite element mesh contained 34,596 nodes and 34,711 elements. For variant 5, it was 38,371 nodes and 39,156 elements. The model in variant 1 – the reference one – contained 30,580 nodes and 30,699 elements. The mesh densities were determined based on a series of numerical tests to establish their convergence.

As a result of numerical analyses, displacement distributions within the studied wall models were determined in the direction normal to

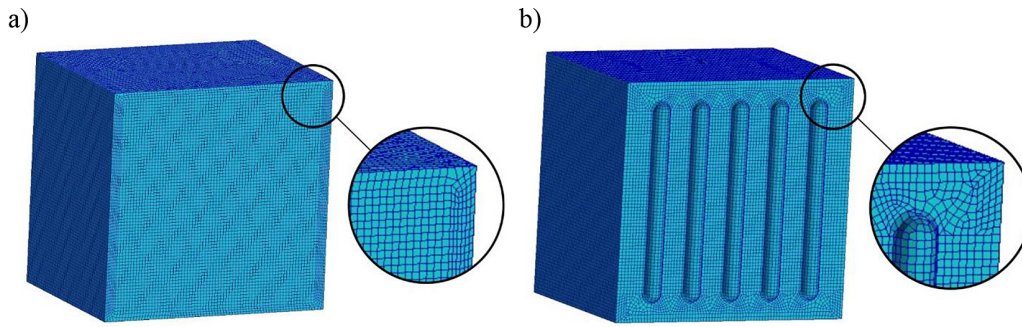


**Figure 15.** Finite element meshes: (a) variant 1, (b) variants 2, 5

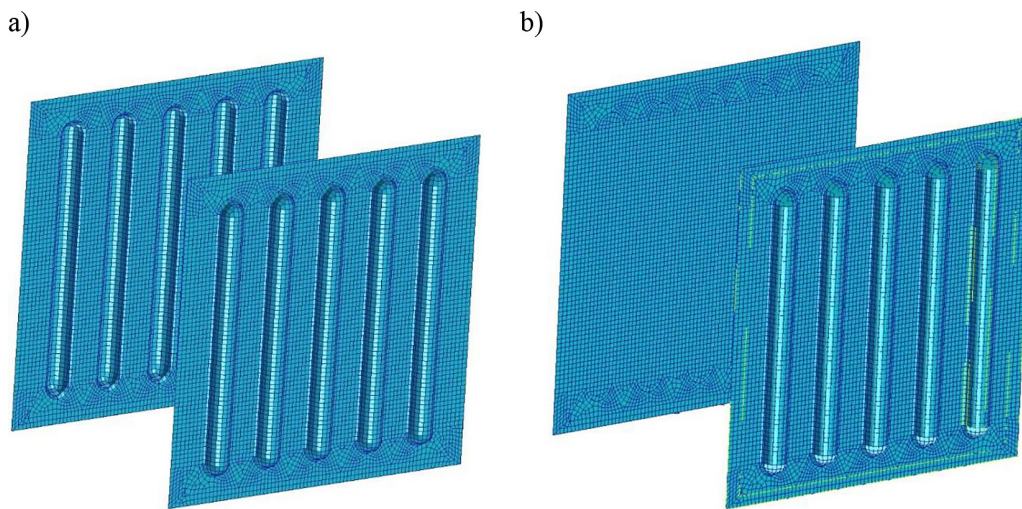


**Figure 16.** Comparison of meshes for models with ribs: (a) variant 2, (b) variant 5

their plane, along with the corresponding reduced stress distributions (Fig. 17–19). Due to the assumption of isotropic material properties, the von Mises hypothesis was employed. Results were also presented for the inner side of the front wall,

highlighting deformations in the closing rib walls and the corresponding distribution of reduced stress (Fig. 20). When comparing the displacement distributions obtained through numerical simulations with the images scanned during the

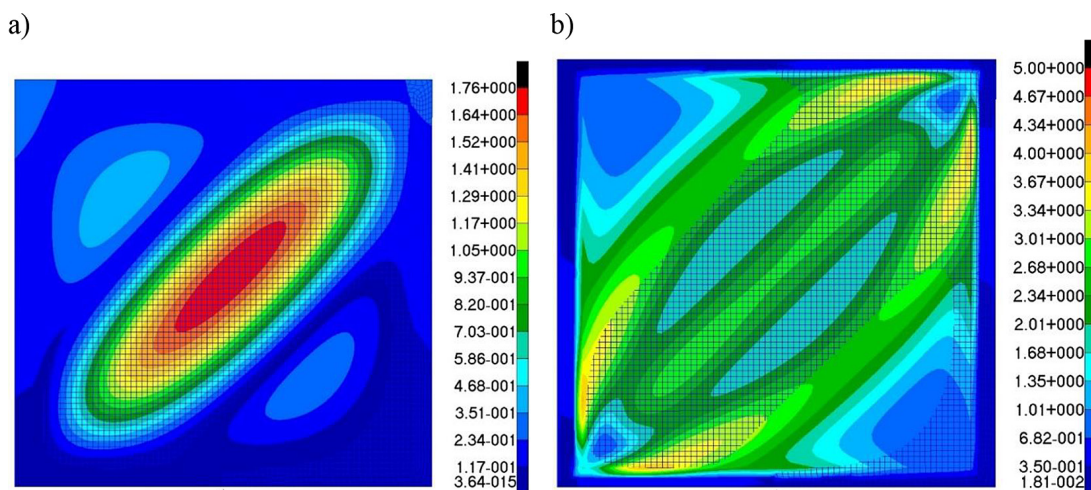


**Figure 17.** Results of numerical analyses for the reference variant: (a) displacement distribution normal to the wall plane [mm], (b) reduced stress distribution according to the von Mises hypothesis [MPa]

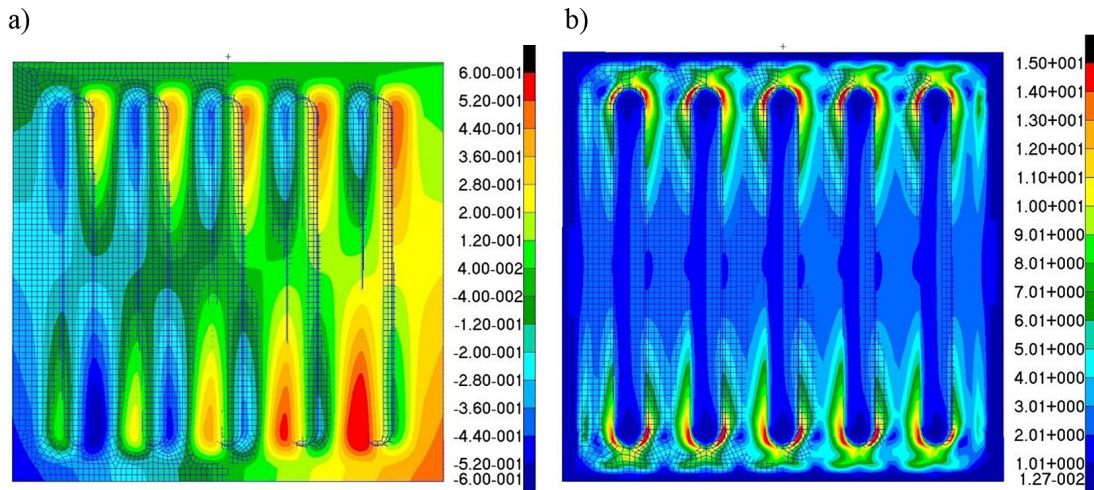


**Figure 18.** Results of numerical analyses for the variant 2: (a) displacement distribution normal to the wall plane [mm], (b) reduced stress distribution according to the von Mises hypothesis [MPa]

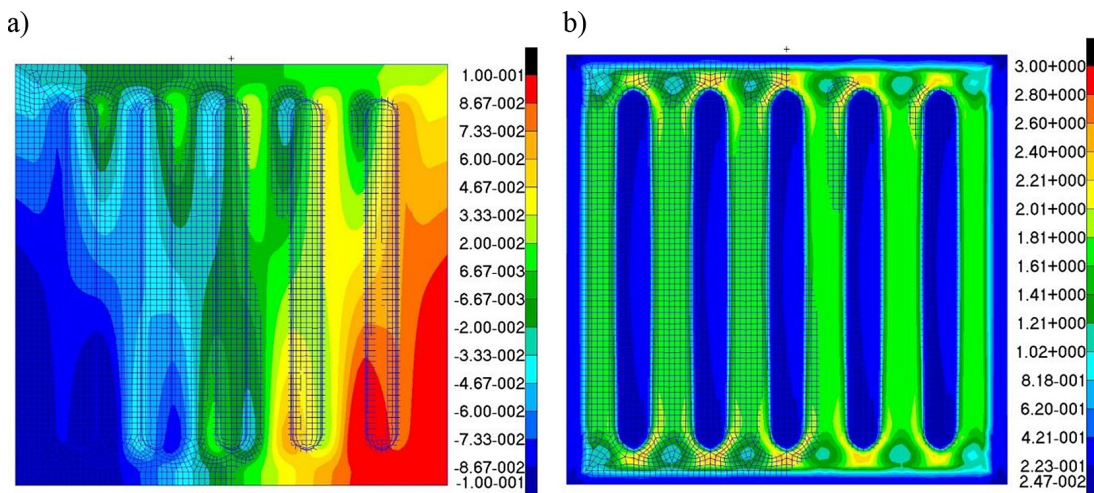


**Figure 19.** Results of numerical analyses for the variant 5: (a) displacement distribution normal to the wall plane [mm], (b) reduced stress distribution according to the von Mises hypothesis [MPa]

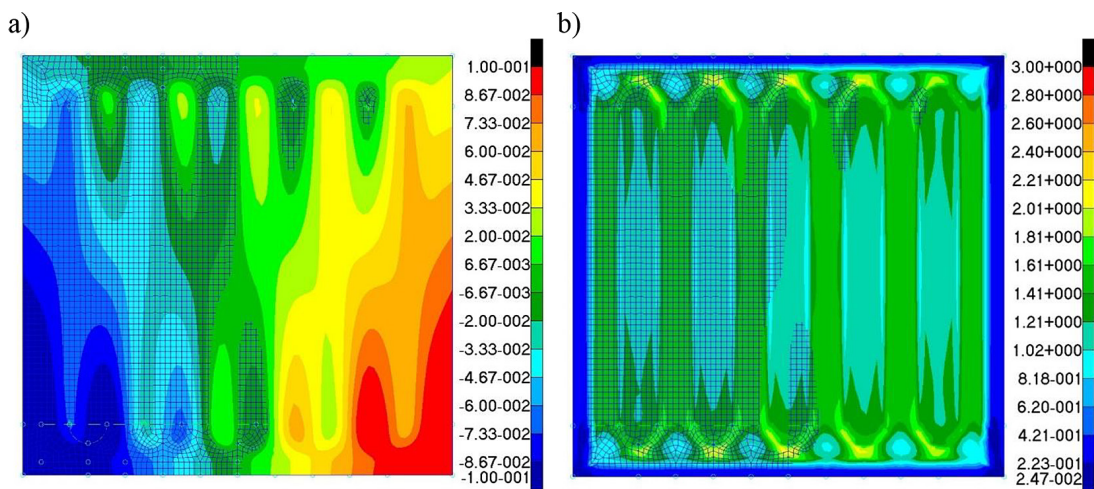


**Figure 20.** Results of numerical analyses for variant 5 inside view: (a) displacement distribution normal to the wall plane [mm], (b) reduced stress distribution according to the von Mises hypothesis [MPa]

experiment, it's essential to consider that they were prepared for different reference systems. In the case of numerical analyses, a common axis system was used for the entire model. However, for the images from the ATOS scanner, displacement distributions were obtained by comparing reference points located in the corners of the wall, for states before and after deformation. These latter points do not account for displacements resulting from the torsion of the entire tested structure.

In this situation, certain quantitative discrepancies seem justified. However, the satisfactory qualitative similarity confirms the adequacy of the numerical models and allows for the assessment of stress distributions. In the case of the reference structure, the distribution of reduced stress corresponded to a typical tension field, with visible zones of tension and compression. Achieving satisfactory agreement in displacement distributions with the experimental results allowed for the assumption of the correctness of the modeling concept and the adequacy of the numerical model. In the case of subsequent versions, modifications only involved the front and rear walls. In the case of variant 2, as expected, the most critical zones showing the highest stress concentrations turned out to be the regions of the wall adjacent to the ends of the ribs. Within the ribs themselves, the values of the reduced stress were approximately 20% of the maximum values, indicating they were of the same order of magnitude.

In variant 5, due to the support provided by the closing walls, which relieves the ribs, the value of reduced stress was an order of magnitude lower than in the concentration zones. Both the displacement magnitudes and stress values in variant 5 were approximately five times lower than in variant 2, due to a significant increase in the torsional stiffness of the ribs after implementing the closed perimeters.

Displacement distributions for the rib-closing walls reveal local zones of instability, the presence of which results in the loss of torsional stiffness of the structure at higher load values. Stress levels in the convex parts of the ribs were approximately five times lower than in the closing walls.

## CONCLUSIONS

The results of experimental studies have demonstrated that the analyzed solutions concerning the use of ribbed structures fabricated using

additive manufacturing techniques helped prevent significant buckling deformations. However, the presence of corrugated ribs with open cross-sections resulted in a reduction in the torsional stiffness of the structure. In the case of variant 2, corresponding to semicircular rib cross-sections, this was a decrease of approximately 75%. For variants 3 and 4, representing flattened ribs, the decrease was approximately 50% and 25%, respectively. Furthermore, these solutions led to an increase in mass of approximately 53% for variant 2, 38% for variant 3, and 25% for variant 4. This suggests that the benefits of employing such solutions are primarily related to a significant increase in critical load levels and can be applied in load-bearing areas where instability is particularly undesirable, such as for aerodynamic reasons. In such cases, as demonstrated by experience, it seems advantageous to use flattened rib cross-sections, which do not contribute to an excessive decrease in the torsional stiffness of the structure or an increase in mass. However, significantly reducing the height of the rib cross-section can lead to a drastic reduction in its effectiveness and the onset of buckling deformations. Precisely determining the geometry of the rib cross-section that provides the maximum benefits from a design perspective requires further detailed research.

A much more promising solution appears to be the use of corrugated ribs with closed cross-sections. In the case of variant 5, the increase in the torsional stiffness of the structure compared to the reference variant was approximately 60%. At the same time, the increase in wall mass compared to variant 2 was only about 13.6%. By employing walls that close off the rib bases (variant 5), the torsional stiffness of the structure was almost 280% higher than in variant 2. With this type of solution, increasing the height of the rib results in an increased closed cross-section perimeter and thereby an increase in torsional stiffness, but it also causes an increase in the structure's mass. Therefore, similar to ribs with open cross-sections, it seems sensible to conduct additional analyses aimed at precisely determining the most optimal geometric parameters of the cross-section.

The issue with the last of the solutions discussed is the decrease in torsional stiffness caused by the buckling of the rib-closing walls. It's important to note that flat walls were used in the presented model, susceptible to buckling. As mentioned earlier, there are several possibilities for shaping the details of the solution, with the simplest being

to increase the thickness of the walls. However, alternative versions of rib cross-sections should also be considered. It is anticipated that these issues will be the subject of further research.

The results of the numerical analyses exhibited satisfactory agreement of displacement values in relation to the experiment. In the case of variant 1, the discrepancy between the maximum values of transverse wall deformation was approximately 6%, whereas for variant 2, it was around 7%. Comparing the conformity of deformations for variant 5 is difficult due to the fact that the displacements resulting from the deformation of the structure as a whole are of the same order as the absolute transverse displacements of the examined walls. However, the overall torsion angles showed agreement, and therefore, considering that all numerical models had identical structures and identical boundary conditions, it can be inferred that the obtained stress distribution results are reliable.

## REFERENCES

- Dayyani I., Shaw A.D., Saavedra Flores E.I., Friswell M.I., The mechanics of composite corrugated structures: A review with applications in morphing aircraft, *Composite Structures* 1 December 2015.
- Bo-Li Z., Wen-Hua B., Chen-Bao W., Jia-Qi Z., Hao-Jun S., Xiong W., Yan-Lin G., Experimental and numerical investigation into hysteretic performance of orthogonal double corrugated steel plate shear wall, *Thin-Walled Structures* 2024, 195: 111392.
- Chen-Bao W., Bo-Li Z., Hao-Jun S., Yan-Lin G., Wen-Jin Z., Li-Lan D., Global stability design of double corrugated steel plate shear walls under combined shear and compression loads, *Thin-Walled Structures* 2024; 199: 111789.
- Shaw A.D., Dayyani I., Friswell M.I., Optimisation of composite corrugated skins for buckling in morphing aircraft, *Composite Structures*, 2015; 133: 358–380.
- Kratochvíl J., Sadilek M., Musil V., Stanceková D., The effectiveness of strategies printing printer easy 3D maker, *Advances in Science and Technology Research Journal* 2018; 12(2): 197–205.
- Dobrzanski P., Czarnocki P., Lorenz Z., *Shell structures – theory and application*, CRC Press, 2013.
- Kopecki H., Kopecki T., Swiech Ł., *Issues of aircraft structural strength*, Rzeszow University of Technology Publishing House, Rzeszow, 2023.
- Monaldo E., Ricci M., Marfia S. Mechanical properties of 3D printed polylactic acid elements: Experimental and numerical insights, *Mechanics of Materials*, 2023; 177: 104551.
- Kopecki T., Świąch Ł., Experimental-numerical analysis of a flat plate subjected to shearing and manufactured by incremental techniques, *Advances in Science and Technology Research Journal* 2023; 17(4): 179–188.
- Felippa C.A., Crivelli L.A., Haugen B. A Survey of the Core-congruent Formulation for Nonlinear Finite Element, *Archives of Computer Methods in Engineering* 1994; 1: 1–48.
- Madier D., *Practical Finite Element Analysis For Mechanical Engineers*, 2020, FEA Academy.
- Doyle J.F. *Nonlinear analysis of thin-walled structures*, Springer-Verlag, Luxemburg 2001.
- Mazurek P., Fatigue strength of thin-walled rectangular elements in the state of post-critical deformation, *Advances in Science and Technology Research Journal* 2019; 13(2): 84–91.
- Swiech, Ł. Experimental and numerical studies of low-profile, triangular grid-stiffened plates subjected to shear load in the post-critical states of deformation, *Materials*, 2019; 12: 3699.
- Tewari K., Pandit M.K., Budarapu P.R., Natarajan S., Analysis of sandwich structures with corrugated and spiderweb-inspired cores for aerospace applications, *Thin-Walled Structures*, 2022; 180: 109812.
- Kopecki T., Swiech Ł., Experimental-numerical analysis of a flat plate subjected to shearing and manufactured by incremental techniques, *Advances in Science and Technology Research Journal* 2023; 17(4): 179–188.
- Monaldo E., Ricci M., Marfia S. Mechanical properties of 3D printed polylactic acid elements: Experimental and numerical insights, *Mechanics of Materials* 2023; 177: 104551.